# Characterizing Sub-Terahertz Reflection and Its Impact on Next-Generation Wireless Networking

Ruiyi Shen, Graduate Student Member, IEEE, and Yasaman Ghasempour, Member, IEEE

Abstract—Owing to the substantial bandwidth they offer, the exploration of 100+ GHz frequencies for wireless communications has surged in recent years. These sub-Terahertz channels are susceptible to blockage, which makes reflected paths crucial for seamless connectivity. However, at such high frequencies, reflections deviate from the known mirror-like specular behavior as the signal wavelength becomes comparable to the height perturbation at the surface of the reflectors. Such reflectors are considered electromagnetically "rough" which results in random non-specular reflection components that are not well understood. In this paper, we delve into the fundamentals of rough scattering to analyze its implications for sub-THz wireless networks, including the existence and strength of non-specular links, mobility resilience, and beam reciprocity. Further, we present a novel framework that re-purposes IEEE 802.11ay-like beam sweeps for estimating the surface roughness of a reflector in the vicinity of the communication nodes. Through extensive modeling, simulation, and experiments with everyday reflector samples, we demonstrate the impact of rough scattering on overthe-air data links and evaluate the accuracy of our roughness inference framework.

Index Terms—Terahertz communications, diffuse scattering, rough surfaces, mobile networking.

#### I. INTRODUCTION

IRELESS communications at frequencies beyond 100 GHz, or the sub-terahertz (sub-THz) regime have received tremendous attention in recent years because of the wide available bandwidth that can support multi-Gbps data rates. In order to counter the high propagation loss of signal, sub-THz wireless communication often utilizes highly directional line-of-sight (LOS) links. However, compared to legacy sub-6 GHz networks, directional wireless links at sub-THz are more susceptible to blockages such as the human body and many common obstacles in the wireless environment [2], [3]. To counter the challenge of LOS blockage, non-line-ofsight (NLOS) links established from the reflection of objects become crucial. Indeed, past research has shown that strong sub-THz reflected links can be established using common everyday surfaces as reflectors, especially in typical indoor wireless environments, at frequencies up to 400 GHz and a data rate of 1 Gb/s. [4], [5].

Conventionally, reflection is modeled with Snell's law which suggests the reflection angle simply equals the incident angle. However, such a well-behaved pattern ignores the height perturbation of the reflector, which is a valid assumption at legacy sub-6 GHz bands. At 100+ GHz frequencies, however, the wavelength drops below 3 mm and becomes comparable to

The authors are with the Department of Electrical and Computer Engineering, Princeton University, Princeton, NJ 08544, USA (email: ruiy-ishen@princeton.edu; ghasempour@princeton.edu). Yasaman Ghasempour is the corresponding author.

An earlier version of this paper was presented in part at the 29th Annual International Conference on Mobile Computing and Networking (ACM MobiCom '23), October 2-6, 2023, Madrid, Spain [1].

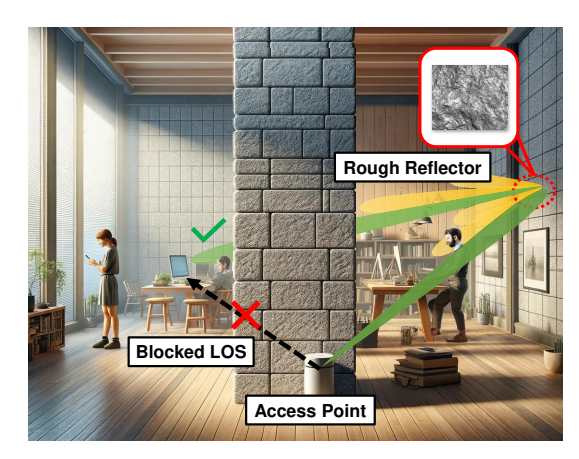


**Fig. 1:** Under LOS blockage, we take advantage of reflection to establish NLOS wireless links. These reflecting surfaces in our surroundings can become electromagnetically rough in the sub-THz band and diffusively scatter the incident signal toward multiple spatial locations.

the minute height variation of common reflectors that ranges from 10  $\mu$ m to a few millimeters [6]. Therefore, natural surfaces that were considered smooth at low frequencies would become *electromagnetically rough* at sub-THz, which can diffusively scatter impinging signals. In case of LOS blockage, as shown in Fig. 1<sup>1</sup>, an alternate NLOS path can be established to maintain the wireless link between different nodes. At sub-THz frequencies, strong diffusively scattered NLOS communication links that do not follow the mirror-like reflection pattern may also be established with a rough reflector, but they are yet to be thoroughly studied.

Previous studies have attempted to model and, to some degree, measure the effects of rough scattering on electromagnetic wave propagation [7], [8]. However, the implications of rough scattering for the control plane have not been thoroughly investigated. This paper aims to address this gap through a comprehensive analysis of rough surface scattering in sub-THz wireless networks and offer insight into new control plane designs. Specifically, we study the impacts of rough scattering on coverage, mobility resilience, and non-reciprocal transmit-receive beams. Furthermore, we introduce a novel framework to estimate the roughness of a reflector, allowing the prediction of reflection profiles in sub-THz wireless networks.

There are two wavefronts from scattering off of a rough surface: a phase-coherent wavefront that propagates near the specular angle, and a non-coherent wavefront that scatters to a wide range of non-specular directions. Fig. 2 depicts two example scattering profiles from smooth and rough surfaces. The rays randomly scattered toward multiple angles in Fig. 2(b) suggests that the non-coherent components increase with

<sup>1</sup>This figure is generated with the assistance of DALL·E 3 from OpenAI.

"rougher" surfaces. Unfortunately, finding exact closed-form solutions for the general electromagnetic scattering problem remains an open challenge as it requires solving boundary conditions throughout each surface individually. Instead, random natural surfaces can typically be modeled by a Gaussian height distribution, with roughness level determined by the standard deviation of height variation and the correlation length across the surface. With such a statistical model, we employ the integral equation model (IEM) to estimate the characteristics of the scattered wavefronts [7].

Through comprehensive simulation and over-the-air experiments, we illustrate the impact of rough surface scattering from various perspectives: First, as surface roughness increases, the reflected power at the specular direction exponentially decays. However, the reflected power is distributed over a wider range of non-specular angles, which benefits link coverage and mobility resilience in wireless networks, as a relatively stable power is expected with moderate client motion. This contrasts directional LOS channels that are vulnerable to sudden link disruptions with slight user motion. Interestingly, because the non-coherent wavefront from rough scattering is incident-angle-dependent, we show that the assumption of transmit-receive beam reciprocity no longer holds for sub-THz NLOS links established with rough surfaces. The lack of beam reciprocity introduces complications in the directional link establishment procedure. In particular, today's IEEE 802.11ay protocol [9] in mmWave WLANs incorporates a sector sweep with a search space of O(N) instead of  $O(N^2)$  by assuming that the best transmit beam at a node is also the best receive beam at that node for a fixed point-to-point link. Our results show that this is not always the case for sub-THz NLOS links.

Given the importance of incorporating reflector roughness into control plane decision-making, we present the first framework that infers the characterization of the NLOS scattering profile of a reflector in the vicinity of access point (AP) and mobile users. Our key idea is that the interference between coherent and non-coherent wavefronts that emerge from reflection from a rough surface imposes a random frequencyselective channel response. Hence, the power variance of the reflection spectra captures the intensity of non-coherent scattering wavefronts and can be mapped to the surface rootmean-square (RMS) height. However, the magnitude of such spectral fluctuation is subject to changes in the environment and typical channel dynamics (e.g. distance, antenna gain, power, motion, etc.). Hence, it is difficult to make reliable inferences from a single reflection measurement. Our insight is to capture and integrate the reflection spectra from multiple incident angles to acquire roughness-rich data. Indeed, the diffuse scattering patterns vary with the angle of incident waves on the reflectors. Yet, physically moving the AP or user equipment (UE) to scan a surface from various angles is unrealistic in communication settings. Instead, we re-purpose the conventional beam sweep procedures primarily used for directional link establishment. Interestingly, we observe that under different beam configurations, the slight changes in the angle of incidence/reflection leave unique fingerprints in the reflection spectra which we leverage for roughness extraction. We emphasize that such beam sweep procedures are already

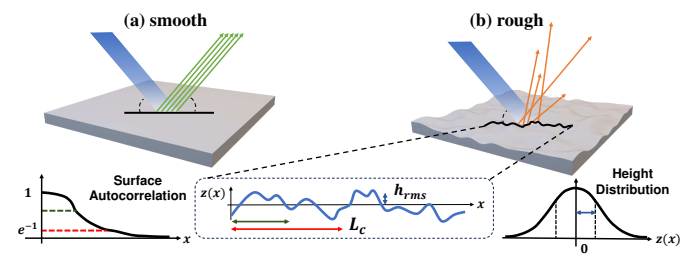


**Fig. 2:** An illustration of the difference between (a) reflection from a smooth surface and (b) scattering from a rough surface.

built into IEEE 802.11ay for 60 GHz WLANs and similar link establishment schemes are expected for sub-THz networks. Further, our framework induces zero additional overhead and is training-free.

We deploy a frequency-multiplier-based data-modulated setup to demonstrate the first over-the-air experimental analysis of a 10 Gb/s NLOS link at 140 GHz established with rough surfaces using quadrature amplitude modulation (QAM). We comprehensively illustrate the important implications of rough scattering in sub-THz wireless networks by analyzing key link quality indicators such as signal-to-noise ratio (SNR) and bit error rate (BER) from links established with typical everyday surfaces including tile, brick, redstone, and granite. In addition, we also deploy a broadband time-based THz system to evaluate the first roughness inference framework from replicating a beam sweep procedure. Our experimental results show that we can achieve an accuracy of 0.107 mm in RMS height estimation, which can significantly help infer scattering beam patterns for sub-THz wireless networking.

#### II. PRIMER IN DIFFUSE SCATTERING

## A. Definition of Surface Roughness

As depicted in Fig. 2, the roughness of a surface refers to the small-scale fluctuations in height across different points. Here, x denotes the horizontal displacement from a reference point on the surface, and z(x) represents the vertical height at position x relative to the mean height. Natural surfaces typically exhibit a Gaussian height distribution with 0 mean. Hence, the probability of encountering a vertical height z(x) at a horizontal location x can be characterized by the Gaussian probability density function with a standard deviation of height variation that we define as RMS height  $(h_{rms})$  [7]:

$$p(z) = \frac{1}{\sqrt{2\pi h_{rms}^2}} e^{-z^2/2h_{rms}^2}.$$
 (1)

**Roughness parameters:** It is important to highlight that  $h_{rms}$  introduced above stands out as one of the most important parameters influencing the diffuse scattering profile of the surface. In addition, another parameter is surface correlation length  $(L_c)$ , which defines the horizontal distance within which the roughness distribution of a surface is considered correlated. As shown in Fig. 2, surface  $L_c$  can be obtained by calculating the maximum length at which the autocorrelation function of a surface height distribution remains above  $e^{-1}$  [7]. Intuitively,  $L_c$  reflects the continuity of the surface height distribution

and serves as a measure of the horizontal roughness of a surface. When  $L_c$  is small, the surface displays significant discontinuities with numerous irregularities, whereas larger values imply a more smoothly continuous variation.

#### B. Roughness Criterion

To evaluate whether a surface is electromagnetically smooth or not, we can consider two scattered rays from separate points on the surface and examine the phase difference between them. For rougher surfaces, the phase difference is expected to be higher as larger surface height variations cause the two rays to travel different path lengths. Rayleigh's criterion states that a surface is considered smooth if the phase difference between two scattered rays is less than  $\pi/2$  [10]. For a random natural surface, this corresponds to

$$h_{rms} < \frac{\lambda}{8\cos\theta_i}. (2)$$

Dependency on frequency and incident angle: One key observation from Eq. (2) is that the roughness criterion changes with both wavelength  $\lambda$  (frequency f) and incident angle  $\theta_i$  of an impinging signal. The first implication is that a surface with a fixed height profile  $h_{rms}$  may be classified as smooth at low frequencies but rough at higher frequencies. In fact, this is the reason why surfaces are assumed to be mirror-like reflectors at sub-6 GHz, while the impacts of surface roughness become significant in sub-THz wireless networks. Note that natural surfaces in everyday indoor/outdoor environments have  $h_{rms}$  values up to the millimeter regime. Meanwhile, according to Eq. (2), surfaces with  $h_{rms} > 530~\mu{\rm m}$  are considered rough at 100 GHz with 45° incidence, which is comparable to the roughness of natural surfaces.

In addition, as the incident angle  $\theta_i$  relative to the surface normal increases, the criterion in Eq. (2) increases. This suggests that a surface can appear rough when approached at angles closer to perpendicular, yet become smooth when approached at angles closer to parallel. This observation holds intriguing implications for wireless networks: the angular location of the TX relative to the surface should be considered when selecting the optimal reflected paths.

# C. Rough Scattering Theory

For a perfectly smooth surface, the reflection of a signal follows Snell's law. This component has a uniform phase front and therefore is called the coherent scattering component. The reflected power can be calculated from the Fresnel equations such that  $P_{ref} = \Gamma_{smooth} \cdot P_{inc}$ , where  $P_{inc}$  and  $P_{ref}$  are the incident and reflected power, respectively, and  $\Gamma_{smooth}$  is the Fresnel reflectivity. However, a non-negligible reflection component distributes power toward other angles from a rough surface, which we refer to as the non-coherent component. Since the total reflected power is conserved, the coherent component along the specular direction experiences a loss that can be written as  $P_{ref} = \Gamma_{smooth} \cdot \rho_{spec} \cdot P_{inc}$ . Here,  $\rho_{spec} < 1$  is the scattering loss factor, or Rayleigh roughness parameter, that is expressed as the following for a Gaussian height distribution [11]:

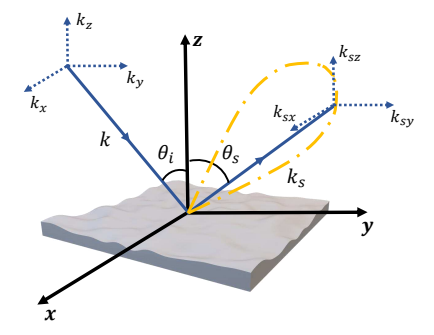


Fig. 3: Basic geometry of scattering model.

$$\rho_{spec} = \exp\left[-8\left(\frac{\pi h_{rms}\cos\theta_i}{\lambda}\right)^2\right]. \tag{3}$$

We observe from Eq. (3) that for a smooth surface with low  $h_{rms}$ ,  $\rho_{spec}$  is close to 1, suggesting that there is a negligible loss in the specular reflection component from scattering. When the roughness increases, the incoherent component takes up more fractions of the power from the incident wave, until the coherent component becomes very small (i.e.,  $\rho_{spec} \ll 1$ ).

Unfortunately, the non-coherent scattering of electromagnetic waves is a random event and has no generalized closed-form solution. However, many approximations of scattering patterns using statistical surface parameters such as RMS height and correlation length have been proposed in the literature [12], [13]. One widely used model is the IEM model, which defines a real-valued scattering coefficient at any arbitrary incident and scattering angles [7], [14]. The model assumes that an incident beam is divided into an infinite array of parallel rays, each of which undergoes a specular reflection with respect to the tangent plane at the point of incidence on the surface. The reflected electric fields are statistically averaged across the illuminated surface area, yielding an approximation of the scattering profile [15].

From the IEM model, the scattering coefficient  $\sigma$  defines the relationship between transmitted and received power under a bistatic setting with incident angle  $\theta_i$  and scattering angle  $\theta_s$ . In general,  $\sigma$  also depends on elevation angles  $\phi_i$  and  $\phi_s$ , but we assume  $\phi_i = \phi_s = 0$  to simplify the equation.<sup>2</sup> The bistatic scattering coefficient  $\sigma(\theta_i, \theta_s)$  can be written as follows [7]:

$$\sigma(\theta_i, \theta_s) = \frac{k^2}{2} \exp\left[-h_{rms}^2(k_z^2 + k_{sz}^2)\right]$$

$$\sum_{n=1}^{\infty} \frac{h_{rms}^{2n}}{n!} |I^n|^2 W^{(n)}(k_{sx} - k_x),$$
(4)

where k is the wave number of the incident wave;  $k_x = k \sin \theta_i$  and  $k_z = k \cos \theta_i$ ;  $k_{sx}$  and  $k_{sz}$  are similarly defined according to  $\theta_s$ , as shown in Fig. 3 [1].  $I^n$  is the n-th power of surface current induced by the impinging electric field expressed as

$$I^{n} = (k_{z} + k_{sz})^{n} f_{k} \exp(-h_{rms}^{2} k_{z} k_{sz}) + \frac{(k_{sz})^{n} F(-k_{x}) + (k_{z})^{n} F(-k_{sx})}{2},$$
(5)

<sup>&</sup>lt;sup>2</sup>Extension to elevation plane is mathematically straightforward.

Here,  $f_k$  is the Kirchhoff field coefficient that describes the superposition of rays reflected from the tangent plane at the local incident point on the surface. As frequency or surface roughness increases, more random constructive and destructive interference between the reflected rays occurs, which implies changes in  $f_k$  patterns that deviate from the specular reflection. In addition, F is a fictitious field component introduced to satisfy the boundary condition at the surface. It complements the Kirchhoff field and therefore is called the complementary field coefficient. Note that both field coefficients also depend on  $\theta_i$  and  $\theta_s$ .

Meanwhile,  $W^{(n)}$  is the surface roughness spectrum, determined by the Fourier transform of the n-th power of the surface correlation function  $\rho(x)$ . For a Gaussian distribution along a single dimension, the correlation function can be written as  $\rho(x) = \exp(-x^2/L_c^2)$ . The full surface roughness spectrum at the n-th order can be expressed as

$$W^{(n)}(k_{sx} - k_x) = \frac{1}{2\pi} \int_{-\infty}^{\infty} \rho^n(x) \ e^{jx(k_{sx} - k_x)} dx.$$
 (6)

From Eq. (4) – (6), the scattering coefficient is a complex function of surface RMS height, correlation length, incident angle, and frequency. Even though it is based on the statistical distribution of surface roughness (i.e.  $h_{rms}$ ), it provides us with important insights into the general trends of changes in the coherent and non-coherent scattering components with respect to the surface as well as incident wave parameters. These insights from the IEM model also shed light on the impact of rough scattering in sub-THz wireless networking, and provide us with a basis for MAC-layer protocol design, as we will discuss in Sec. III. Note that the IEM model can also be generalized to backscattering by setting  $\theta_s = -\theta_i$ . This scenario is particularly interesting to numerous sensing applications where a monostatic setup (i.e., TX and RX colocated) is preferred.

# III. IMPACT OF ROUGH SURFACES IN SUB-THZ WIRELESS NETWORKS

So far, we presented the mathematical foundations of scattering from rough surfaces. Next, we delve into the impact of rough surface scattering on sub-THz wireless communication networks. In particular, the wider angular distribution of power and asymmetric incident and scattering angles have important implications in NLOS non-specular paths, mobility resilience, and beam reciprocity. Hence, next-generation wireless networks should account for rough scattering in control plane designs for mobility management, beam selection, and more.

#### A. SNR at Specular and Non-Specular NLOS Paths

The sub-THz channels are known to be LOS dominant. The NLOS paths are generally weaker due to increased path lengths and reflection loss. Prior works have demonstrated the possibility of NLOS connectivity above 100 GHz [16], [4], but have mostly ignored the impact of surface roughness. Hence, as a first step, we characterize the amount of received power

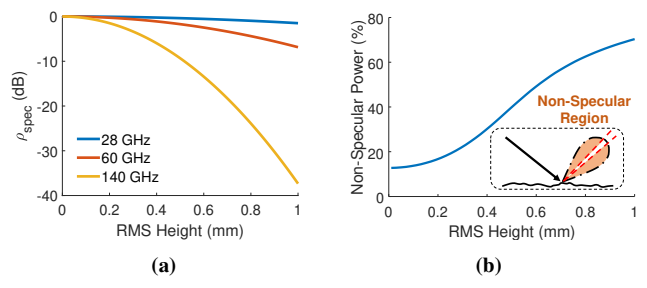


**Fig. 4:** (a) Amount of power loss due to scattering at the specular angle; (b) Percentage of power distribution to non-specular angles.

from specular and non-specular paths as a function of surface roughness. In general, smooth surfaces reflect signals toward the specular direction where maximum SNR is observed. Yet, SNR rapidly drops at non-specular angles. On the other hand, signals scattered off of rough surfaces have lower peak specular SNR, but communication links of comparable strengths can be established at non-specular angles.

To investigate this trend, we first observe the impact of rough surface scattering on specular power. As defined from the modified reflectivity in Eq. (3),  $\rho_{spec}$ , or the scattering loss factor, is a direct representation of reflected power. Hence, Fig. 4(a) illustrates the exponential drop in specular power as a function of  $h_{rms}$  for specular angles  $\theta_i = \theta_s = 45^\circ$  at different frequencies. We note that the drop of specular power from rough surfaces due to diffuse scattering at 140 GHz can be very significant given  $h_{rms}$  within 1 mm for natural surfaces. On the other hand, such impact is less significant for common mmWave bands such as 28 GHz and 60 GHz. In Sec. VI, we experimentally demonstrate the power at specular angles given surfaces at various roughness levels.

Next, we exploit the IEM model to investigate the trend for the non-coherent scattering components. It is evident from Eq. (4) that the non-coherent scattering coefficient is a nonlinear function of surface roughness parameters. Note that the scattered power can be directly calculated from  $\sigma$  using the Friis radar range equation. When comparing the scattered power in a fixed setting, all parameters except  $\sigma$  remain the same. Hence, in the rest of the analysis, we will directly interpret changes in the scattering coefficient  $\sigma$  as changes in SNR.<sup>3</sup> To better understand this dependency, we observe how much power is distributed toward non-specular angles as the roughness of a reflector increases. Specifically, we consider a signal at 140 GHz impinging on a reflector at  $\theta_i = 45^{\circ}$ , and then we define the angles within  $\pm 2.5^{\circ}$  of the specular angle to be the specular range (i.e.  $\theta_s = 42.5^{\circ} - 47.5^{\circ}$ ). Next, we observe the percentage of power distributed outside the specular range, as shown in Fig. 4(b). Evidently, for smooth surfaces, most reflected power is focused toward  $\theta_s = 45^{\circ}$ . However, as  $h_{rms}$  increases, more power distributes toward the non-specular angles, up to 70% at  $h_{rms} = 1$  mm. In practice, depending on the random distribution of surface height, it is also possible to have scattered power at non-specular angles larger than the specular power. Unfortunately, this trend is not

 $^3{\rm Note}$  that  $\sigma$  can have a magnitude above 0 dB, but that does not mean  $P_r/P_t>1.$ 

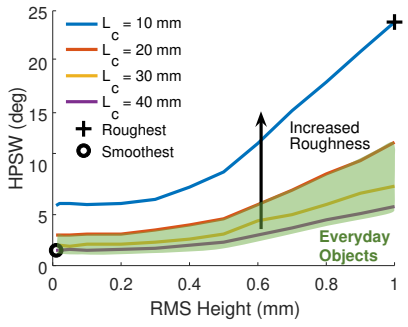


Fig. 5: The Half Power Scattering Width (HPSW) of an NLOS path vs. surface roughness parameters  $h_{rms}$  and  $L_c$ .

captured by the IEM approximation. We will experimentally analyze non-specular scattering patterns in Sec. VI.

The power at the specular angle is highly sensitive to surface roughness at 100+ GHz. In addition, specular paths generally remain stronger, but for rougher surface profiles, more power is distributed to non-specular angles, suggesting the possibility of establishing non-specular links with comparable SNR in future sub-THz wireless networks.

#### B. Resilience to Mobility

One of the main challenges of mmWave and sub-THz wireless links is their sensitivity to mobility from high beam directionality. Intuitively, this applies both to LOS paths and reflected paths off smooth surfaces because the directional beam is maintained after reflection toward the specular angle. In contrast, rough surfaces distribute non-negligible power to non-specular angles. Hence, we expect more resilience against mobility with NLOS links established with rough surfaces.

To investigate this hypothesis, we define *Half Power Scatter*ing Width (HPSW) as the largest difference between scattering angles with less than 3 dB power loss (relative to power at the specular angle). Using the IEM model from Eq. (4), we plot HPSW as a function of surface roughness parameters in Fig. 5. We observe three interesting trends: First, at a fixed correlation length, the scattering width increases monotonically with surface RMS height. The smaller  $L_c$  is, the faster HPSW increases with  $h_{rms}$ . Second, for a surface with high  $h_{rms}$ , the reflected signal can still be very directional (having HPSW of within  $5^{\circ}$ ) given that it is horizontally smooth ( $L_c$ is high). In contrast, a broad diffuse scattering pattern can also be seen on surfaces with low  $L_c$  and low  $h_{rms}$ . Lastly, HPSW remains constant at low  $h_{rms}$  values, and starts increasing at RMS heights larger than Rayleigh's criterion (0.38 mm at 140 GHz) when a surface is classified rough.

Further, from the IEM model, the scattering pattern (and correspondingly HPSW) is dependent on a combination of  $h_{rms}$  and  $L_c$ . For horizontally rough surfaces with low  $L_c$  values, the effect from correlation lengths on scattering patterns dominates over that from  $h_{rms}$ . However, moderate or large correlation lengths contribute minimal changes in rough scattering behaviors. We note that the  $L_c$  of a surface relates to the spot size. Statistically, a smaller spot size leads to a smaller correlation length as it examines the local curvature of an object's surface. On the other hand, a sufficiently

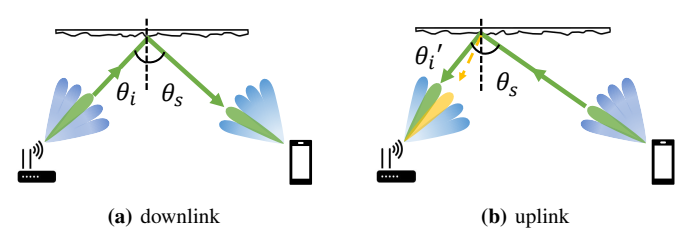


**Fig. 6:** Non-reciprocity in downlink and uplink beams for an NLOS non-specular link established with rough surfaces.

large spot size captures the global surface perturbation profile and usually guarantees a larger  $L_c$ . Even though sub-THz communication signals are directional, the pencil-like beam creates a large area of illumination compared to the small-scale surface perturbation, which comprehensively captures the global roughness distribution of most natural surfaces. Therefore, natural surfaces in everyday wireless environments have comparatively large  $L_c$  values. Hence, the scattering broadening is dominated by the RMS height profile, shown with the shaded area in Fig. 5 [17], [18]. Consequently, we treat  $h_{rms}$  as the major parameter that affects the scattering width and provide a framework to estimate  $h_{rms}$  from spatial-spectral signatures in Sec. IV-C.

Rough surfaces can realize wider reflection patterns at the cost of a weaker specular path, which hints at a tradeoff between link resilience and achievable data rate in highly directional NLOS links. In addition, the RMS height of natural surfaces dominates changes in the rough scattering pattern and can provide additional insights into NLOS sub-THz links.

#### C. Non-Reciprocal Uplink/Downlink Beams

In today's wireless networks, the uplink and downlink beams are assumed to be reciprocal [19]. The reciprocity assumption has been leveraged in various aspects of wireless networks. For instance, beam training is typically performed for either transmission or reception and the conventional wisdom is that, at least for calibration-free arrays, the best beam configuration at the AP to transmit data to a client is the same as the best beam to receive data from the same client. Because of this simplifying assumption, the link establishment overhead was reduced from  $O(N^2)$  to O(N) in IEEE 802.11ay standards, and even commercial mmWave devices [20], [9].

Unfortunately, this assumption might not hold in sub-THz wireless networks with electromagnetically rough reflectors. As depicted in Fig. 6, the best beam configuration at the AP for transmitting data to a client can differ from that for receiving data from the same client [1]. The main reason according to the scattering theory is that the non-coherent scattering wavefront depends on the incident angle. Note that the channel between the AP and the client remains reciprocal because every ray can be traced back following the same propagation path to its origin. However, the surface perturbation profile seen by the incident beam from different angles varies. This contributes to the random superpositions of reflected phase fronts that can generate different scattering responses. In principle, a reciprocal beam should satisfy  $P_r(\theta_i, \theta_s) = P_r(\theta_s, \theta_i)$ , or  $\sigma(\theta_i, \theta_s) = \sigma(\theta_s, \theta_i)$ . However, this is not accurate according

to the IEM model in Eq. (5) because the Kirchhoff field coefficient  $f_k$  is not a symmetric function of  $\theta_i$  and  $\theta_s$  and can yield to a different value in case of downlink vs. uplink. We will experimentally show in Sec. VI that higher  $h_{rms}$  leads to a larger discrepancy between downlink and uplink beams.

The long-standing assumption of beam reciprocity that has inspired overhead-efficient protocols for channel sounding and beam management may no longer hold above 100 GHz. Therefore, it is crucial for future wireless networks to take reflector characteristics into account.

#### IV. SURFACE ROUGHNESS ESTIMATION

Thus far, we have illustrated that surface roughness has critical implications for various aspects of sub-THz wireless networking. Hence, a natural question arises: how do we estimate the surface roughness of reflectors at the AP and mobile clients? We note that measuring the exact surface profile (e.g., via microscopic imaging) is not feasible or required. Instead, it is sufficient to acquire the statistical roughness parameters for understanding the reflection profile and adapting the control plane protocols in sub-THz networks.

#### A. Roughness Estimation via Exhaustive Scan

According to the scattering theory discussed in Sec. II, there exists a relationship between estimated received power from scattering off of a surface and its roughness parameters (i.e.,  $h_{rms}$  and  $L_c$ ). Therefore, a naive approach is to compare the received power with the theoretical scattering model with Friis radar range equation. In particular, an optimization framework can be formed to find  $h_{rms}$  and  $L_c$  as follows:

$$\underset{h_{rms}, L_c}{\operatorname{argmin}} \left\| \frac{P_r}{P_t} \frac{4\pi^3 R_t^2 R_r^2}{G_t G_r \lambda^2 \iint dA} - \sigma(\theta_i, \theta_s) \right\|^2. \tag{7}$$

However, several issues make this approach impractical: First, the received power is a function of TX and RX distances from the reflector, the area of illumination, the materialdependent reflection coefficient, and antenna directivity gains. Accurate knowledge of these parameters is difficult to acquire in practice. In addition, a single power measurement can be subject to high error when compared with the IEM model. Specifically,  $\sigma(\theta_i, \theta_s)$  characterizes the reflection coefficient of a single scattered ray at certain incident and scattering angles. Yet, in practice, the receiver would capture multiple rays incident at different points on the surface for an NLOS wireless link. Therefore, the random phase from each scattered component can affect the overall superposed profile that is not captured in the model. Nevertheless, the interference from the random phases from each ray provides new avenues for surface roughness estimation that we will leverage in Sec. IV-C.

#### B. Impractical Ultra-Wideband Roughness Estimation

Here, we explore the possibility of using the first-principle model to estimate  $h_{rms}$ . Specifically, according to Rayleigh criterion in Eq. (2), for any surface with a fixed  $h_{rms}$ , we can find a frequency beyond which the surface is classified rough as  $f > f_{rough} = c/(8h_{rms} \cos\theta_i)$ . Intuitively, if a wideband

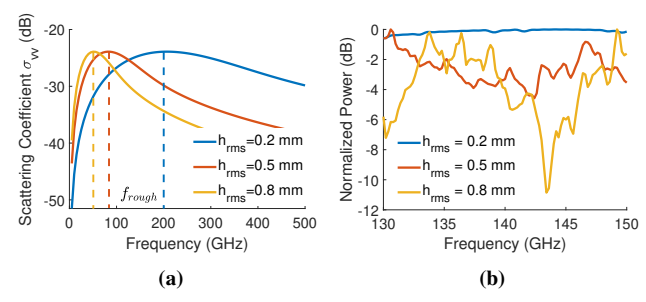


**Fig. 7:** Examples of (a) ultra-wideband reflection spectra from the IEM model, and (b) simulated practical narrowband specular reflection spectra for surfaces with different RMS heights.

spectral response of the surface is available, we expect to observe different behaviors at frequencies below or above  $f_{rough}$ . Fig. 7(a) shows the wideband reflection spectra of three rough surfaces obtained from the IEM model. Indeed, as frequency increases, an increase in directivity leads to higher reflected power for smooth surfaces. However, at frequencies beyond  $f_{rough}$ , the impact of rough scattering begins to dominate, leading to a trend transition and, subsequently, a gradual decrease in scattering coefficient  $\sigma$ . We observe that the spectrum for each rough surface shows a transition at a different frequency. By carefully analyzing the wideband specular reflection spectra with the IEM model, we can extract the transition frequency  $f_{rough}$  for each surface with different  $h_{rms}$ . We also find that the empirically obtained  $f_{rough}$  from the IEM model matches the trend calculated from Eq. (2) as well as that extracted from EM simulations reasonably well. Their agreement allows us to map each observed  $f_{rough}$  to a unique  $h_{rms}$  value. We further validated the robustness of our model in Sec. VI-D with results from over-the-air measurements. However, such a solution requires ultra-wide continuous bandwidth on the hundred-GHz scale, which is not available even for next-generation 100+ GHz wireless networks. For instance, the D-band, identified as a promising candidate for 6G mobile communication, covers certain bands within 130 - 174.8 GHz with a total available bandwidth of 31.8 GHz [21]. Despite the wide bandwidth required, this method provides opportunities for accurate one-shot roughness estimation for sensing applications such as surface profiling and defect detection.

## C. Few-Shot Roughness Inference via Spectral Variance

Hence, we seek a practical and resource-efficient solution to estimate surface RMS height for sub-THz wireless networks. Specifically, leveraging the narrower available bandwidth in sub-THz wireless networks still provides opportunities for roughness estimation. As discussed in Sec. II, the reflection from a rough surface consists of a coherent wavefront and a random non-coherent wavefront. These two components may add up constructively or destructively at various frequencies, leaving a distinct footprint in the received power spectrum. For rougher reflectors, the amount of power scattered in the non-coherent wavefront increases, leading to more random spectral perturbations. On the high level, the amount of power-frequency fluctuation can be an indicator of surface roughness.

Intuitively, the reflected spectra for smooth surfaces are expected to be more uniform while more random perturbations can be seen from that for rougher surfaces.

As discussed in Sec. IV-B, the wideband reflection spectrum for surfaces with different RMS heights provided by the IEM model accurately captures the overall frequency-selective trend for rough scattering. However, the model considers the statistical distribution of surface roughness, which averages the interference between different phase fronts. Therefore, the small-scale reflected power fluctuations at different frequencies that we need for roughness estimation at small bandwidths become hidden under the overall envelope from the model. Instead, to investigate this hypothesis, we fill the gap by performing comprehensive EM simulations. We first create random surface profiles with designated  $h_{rms}$  values. To do so, we draw a 2D matrix of random heights H(x,y) from a Gaussian distribution with a mean value of 0 and standard deviation of  $h_{rms}$  to represent the random heights of a surface at coordinates (x,y). We then apply a Gaussian smoothing filter with a standard deviation of  $L_c$ . We conduct extensive EM simulations for each sample in CST Studio to capture their reflected spectra for a specular reflection at  $\theta_i = \theta_s = 45^{\circ}$ . We first assume plane wave incidence on the reflector sample, and take advantage of the asymptotic solver based on ray-tracing techniques because of its reasonable accuracy and computational efficiency. We observe and capture the far-field bistatic electric field patterns from the reflectors, similar to calculating the bistatic radar cross-section for each sample object. The same simulation is repeated between 130 and 150 GHz with 0.2 GHz resolution, after which we gather and normalize the electric field magnitudes at the specular reflection angle to produce a reflection spectrum for each surface (i.e., normalized reflected power vs. frequency). Examples of specular reflection spectra for different surface models with  $h_{rms} = 0.2, 0.5,$  and 0.8 mm are shown in Fig. 7(b). Clearly, a higher level of signal fluctuation over frequency is observed for rougher surfaces while the spectrum for the smooth surface demonstrates a more uniform trend. We observed that for the surface with  $h_{rms} = 0.8$  mm, the power at different frequencies varies over 10 dB at the maximum. This implies high frequency selectivity due to random interference between wavefronts for extremely rough surfaces. Note that the exact shape and peak/dip location of frequency fluctuation varies significantly from surface to surface, but the average magnitude of variation remains similar for surfaces at the same RMS height, which enables roughness estimation. The singularity of the scattering profile for each surface further motivates the study of rough surface scattering for sub-THz NLOS communications, such as efficient surface height profile imaging for more accurate scattering characterization.

While our feasibility simulations show a trend between roughness and spectral perturbation, quantifying and modeling such a relationship is not straightforward. The power variance across frequency depends on roughness and other factors including the reflector materials and the wireless channel dynamics. Hence, reliably inferring the contribution of roughness on the spectral perturbation in one-shot is very challenging in practical settings. Instead, we leverage the existing beam

sweep procedures and interrogate the target reflector from multiple angles. Therefore, through multi-shot measurements, we aim to capture the unique roughness signatures with the material properties and free-space path loss remaining constant under different beam configurations.

Specifically, we examine the surface with multiple directional beams at different incident angles. The spectra received under various beam configurations (i.e., incident angles) experience similar antenna gains and path losses. Nevertheless, each incident beam illuminates a slightly different area on the surface. Because of the uniform distribution of height profile for natural surfaces with large correlation, the  $h_{rms}$  for neighboring incident areas are considered the same, and therefore, the patterns of the received spectra are also similar. Meanwhile, calculating the mean variance of the received reflection spectra across these spatially diverse links can indicate surface roughness.

Fig. 8 illustrates our framework. As shown, a beam sweep involves sending known beacons across predefined directions while the other node is configured to a quasi-omnidirectional pattern to receive and analyze these beacons. Examples of such procedures are already standardized in IEEE 802.11ay for mmWave WLANs [22], [9]. Conventionally, the receiving node assesses the received signal strengths (RSS) of each beam and finds the best beam that provides maximum RSS. Instead of merely analyzing RSS for beam selection, our key idea is that surface roughness leaves spectral footprints in the power spectra of the received beacons. For rougher surfaces, the noncoherent scattering component contributes to the increased fluctuations in the spectral band. Hence, the magnitude of spectral variance from strong NLOS beams is an indirect indicator of the intensity of the non-coherent wavefront from interference between different phase fronts. This means that evaluating the spectral reflection response from strong NLOS beams can accurately infer the roughness of the reflector.

To leverage such spectral information, we first distinguish NLOS beams from LOS beams using common techniques including time of arrival and received power. Among the NLOS beams, we identify the beam that captures the highest power as it carries the richest scattering-related information. This beam usually lies at or close to the specular direction, but can also be at non-specular angles, especially for very rough surfaces that offer non-specular links of comparable or even larger power. Here, because of the large aperture size for common natural surfaces compared to the wavelength at 100+ GHz frequencies, it is reasonable to assume that a specular NLOS path always exists. Next, we look for the range of neighboring beams that experience at most a 3-dB power drop from the peak. In this way, we make sure that we are not evaluating the spectrum of noise. In addition, we require no prior information on the incident angle because the group of beams selected can either be in the specular or non-specular angles. Then, we take the FFT of the previously identified NLOS beams and calculate the Mean Spectral Variance (MSV) with the normalized spectra to infer roughness. Specifically, we denote  $R_k(f)$  as the frequency-domain received signal under the kth beam. We denote the beam indices with 3 dB of power drop on two sides of the max-power beam

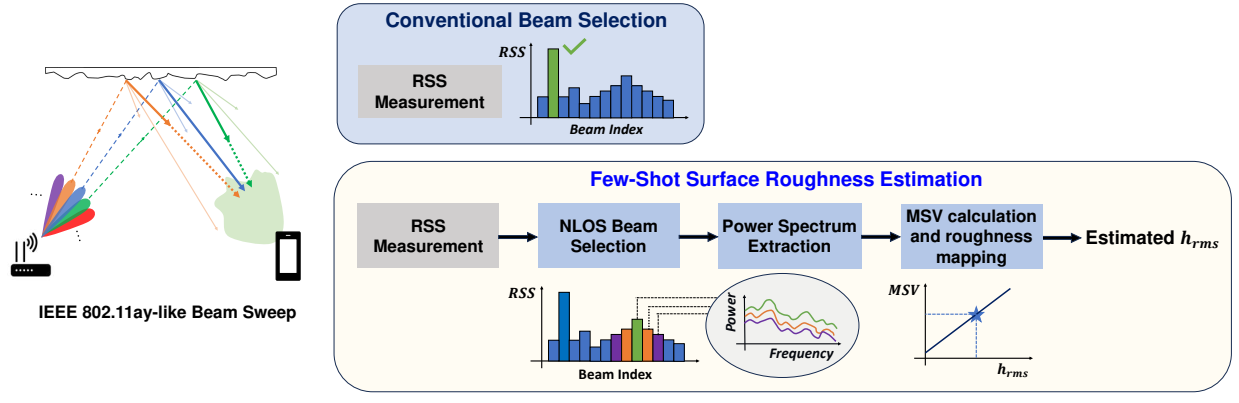


Fig. 8: Our few-shot roughness inference architecture. We analyze the mean variance for spectral profiles of the received beacons under different incident beam configurations (angles) to estimate surface RMS height.

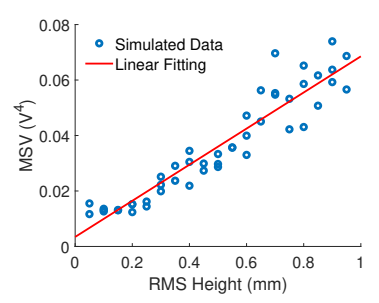


Fig. 9: Mapping between mean spectral variance (MSV) and surface  $h_{rms}$  for NLOS beams. A linear fit is applied to model the relationship between the two, which enables surface roughness estimation.

(can be at the specular or non-specular angles) as  $k_{min}$  and  $k_{max}$ , respectively. Hence, k should fall in the range of  $k \in \mathbf{K} = \{k_{min},...,k_{max}\}$ . We define MSV as follows

$$MSV = \frac{1}{|\mathbf{K}|} \sum_{k \in \mathbf{K}} Var_f \left[ \frac{\mathbf{R}_k(f)}{||\mathbf{R}_k||} \right], \tag{8}$$

where  $|\mathbf{K}|$  is the cardinality of the set of examined beams,  $f \in \{f_c - BW/2, f_c + BW/2\}$ ,  $f_c$  and BW are the center frequency and bandwidth, respectively.

We exploit MSV as a metric to infer surface roughness. Intuitively, under a smooth surface, the coherent reflection component dominates. Therefore, the randomness in scattering and the fluctuations in its received power spectrum are minimal, and MSV is small. On the other hand, MSV is expected to increase with surface  $h_{rms}$ . To demonstrate the exact relationship between MSV and RMS height, we conduct extensive EM simulations with surface roughness  $h_{rms}$  ranging from 0.05 to 0.95 mm. In Fig. 9, we plot the captured MSV values against  $h_{rms}$ . We observe that MSV monotonically increases with  $h_{rms}$  in a near-linear manner. Therefore, as a first-order approximation, we can construct a mathematical model between the two by simply applying a linear fit, where we obtain the following relationship:

$$MSV = 0.0651 \cdot h_{rms} + 0.0034. \tag{9}$$

From the simulated surfaces, this model achieves a mean absolute error in  $h_{rms}$  of 0.0757 mm, and a median absolute

error of 0.0541 mm, which justifies the high quality of the fitting as well as the robustness of our roughness estimation framework. Note that the range of MSV is numerically small, between 0 and 0.08. This is because each spectrum is normalized to 1  $(V^2)$ . Mathematically, the variance of a sequence considers the square of the difference between each number and its mean value. Therefore, if all numbers in a sequence are smaller than 1, the variance will also be numerically small from squaring numbers below 1. Overall, MSV is a statistical representation of the level of perturbation of a reflection spectrum, and its numerical range does not affect the accuracy of our roughness estimation scheme.

Impact from Bandwidth. Since we map the spectral perturbation to roughness, a wider bandwidth is desired as it carries richer spectral information. In the previous analysis, the simulation takes into account 20 GHz of bandwidth. We emphasize that such wideband transmission is needed at coarse time scales for reflector characterization and environmental mapping. The data transmission phase can exploit narrower bands. Nevertheless, we investigate the robustness of our roughness estimation scheme under narrow-band scenarios. We repeat our analysis under narrower bandwidths of 5 and 10 GHz centered at 140 GHz. We note that today's 60 GHz WLANs can support up to 8 GHz of bandwidth [23], and even wider bandwidths are expected in 6G wireless networks [24]. Fig. 10 shows the result. We find that with a bandwidth of 10 GHz, a clear relationship between MSV and RMS height can be observed and a mathematical model can be constructed. A mean absolute error of 0.121 mm can be achieved with a linear fitting, higher but comparable to the case where 20 GHz of bandwidth is used. Further, we observe that with a bandwidth of only 5 GHz, a coarse differentiation between smooth surfaces (low MSV) vs. rough surfaces (high MSV) is possible, which can provide important insights into selecting reflectors for optimal NLOS link performance in 100+ GHz wireless networks.

We highlight that our scheme only takes into account power measurements (albeit across frequencies) and not the phase of the signal. Hence, this is a *non-coherent* roughness estimation approach which avoids the challenges in acquiring accurate and reliable phase information above 100 GHz. In addition, the above approach assumes that several TX beams would impinge

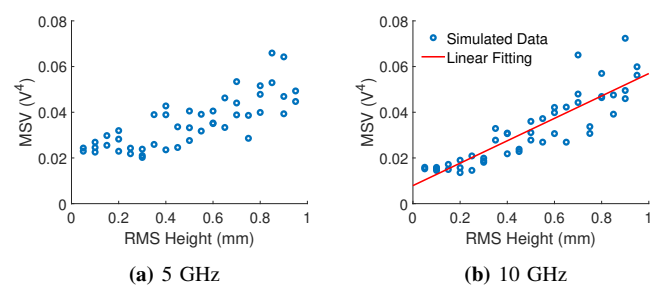


Fig. 10: The spectral variance for different surface models under narrower bandwidths. A clear relationship between MSV and  $h_{rms}$  can be seen with 10 GHz of bandwidth, while coarse differentiation between smooth and rough surfaces is possible even with 5 GHz of bandwidth.

on the reflector of interest, which is a reasonable assumption as practical reflectors (walls, cabinets, etc.) have large apertures. Further, the wireless medium can be a superposition of the LOS path (if unblocked) and other reflected paths. We argue that with highly directional beams at sub-THz, the likelihood of a single beam capturing multiple physical paths is quite small. For instance, a beamwidth of 3.7° has been reported with CMOS phased arrays at 140 GHz as well as with leaky wave antennas [25], [26], [27]. Therefore, we can assume that every beam captures at most one path. Further, distinguishing the LOS beam from NLOS beams is straightforward as LOS beams have significantly higher RSSs and smaller time of arrivals [28]. There has been an extensive line of work on multipath extraction in the literature that applies to our work for the identification of NLOS beams.

We validate our roughness estimation framework with overthe-air experiments in Sec. VI.

#### V. EXPERIMENTAL METHODOLOGY AND PLATFORM

We conduct extensive over-the-air experiments to characterize the impact of rough surfaces on THz wireless networks and evaluate our non-coherent surface characterization approach. We chose 12 different surface samples common in indoor and outdoor environments: ceramic tile, brick paver, redstone paver, and granite block. In addition, we used 3 metal samples as references for each roughness category, including 2 custom 3D-printed rough surfaces. To find the ground truth surface profile, we obtain high-resolution 3D images using the Keyence VK-X3050 surface profiler for an area of 3.5 cm × 3.5 cm at the center of incidence with a resolution of 0.01  $\mu$ m. Examples of surfaces and their 3D models are shown in Fig. 11(a). The surfaces'  $h_{rms}$  values are calculated from microscopic images shown in Table I. Further, we also show the calculated Rayleigh roughness parameter  $\rho_{spec}$  from Eq. (3) at 140 GHz in this Table. Due to the limited spot size of the 3D profiler, the ground truth correlation length  $(L_c)$ calculations are not reliable and we use  $h_{rms}$  as the primary metric of surface roughness.

For over-the-air data transmission and reception, we deploy a frequency-multiplier-based setup shown in Fig. 11(b). On the TX side, a 25 GHz arbitrary waveform generator (Keysight M8195A) is used for generating modulated baseband/intermediate frequency (IF) signal. The local oscillator

(LO) signal is generated by a 67 GHz analog signal generator (Keysight E8257D). Both the IF and LO signals are fed into a compact up-converter module from Virginia Diodes, Inc. (VDI), which consists of two frequency doublers that provide a total multiplication factor of 4×. The up-converted signal is radiated from a WR-6.5 horn antenna by VDI that operates at the D-band between 110 and 170 GHz, which is identified as a candidate for 6G mobile communications. Similarly, on the RX side, a separate horn antenna and down-converter from VDI recover the IF signal with an LO reference that is provided by a separate signal generator of the same model. The down-converted signal is then fed into a 25 GHz real-time oscilloscope (Keysight UXR0254B) for data analysis.

In this setup, the sub-THz signal impinges on the center of the surface sample. Meanwhile, the detector is configured to radially move with respect to the point of incidence on the surface. Both TX and RX are configured to be vertically polarized, and placed at the same elevation height. We measure the reflection profile off of various surfaces at different azimuth configurations.

Because of the limited available bandwidth from the data-modulated setup, we deploy a separate broadband THz time-domain system (TeraMetrix T-Ray 5000) to capture the full scattering response from rough surfaces, as shown in Fig. 11(c). The system produces an ultra-short pulse with a flat frequency response between 100 and 400 GHz. The broadband detector measures the received signal magnitude up to 5 THz with a spectral resolution of 1.22 GHz. The TX and RX are similarly configured to our data-modulated setup.

Note that both of our setups are ultra-low power. Hence, we are limited to table-top measurements at ranges up to 1 meter. However, our observations, insights, and conclusions apply to larger distances. At larger TX-surface distances, the beam spot size on the surface increases; hence, a larger surface area is illuminated and contributes to the total scattering response.

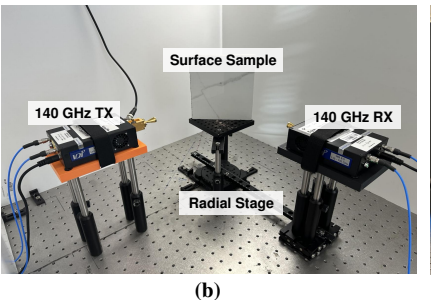
#### VI. EVALUATION

#### A. Data Transmission over Reflected Paths

We first experimentally investigate the scattering from different surfaces at both specular and non-specular angles. Here the TX and RX are placed on two sides of the surface normal. We configure the TX to point to the surface at a fixed 45° angle of incidence, while the RX is moved in a radial pattern to the

TABLE I: Selected samples and roughness parameters.

Sample	ID	$h_{rms}$ (mm)	$ ho_{spec}$
Metal Sheet	1	0.011	0.999
Ceramic Tile	1	0.051	0.978
	2	0.083	0.943
	3	0.064	0.965
3D Printed Metal	1	0.276	0.520
Brick Paver	1	0.224	0.649
	2	0.303	0.454
	3	0.323	0.408
Redstone Paver	1	0.370	0.308
	2	0.377	0.295
	3	0.264	0.549
3D Printed Metal	2	0.659	0.233
Granite Block	1	0.748	0.008
	2	0.902	0.001
	3	0.610	0.041



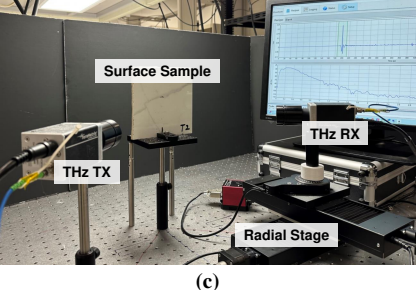


Fig. 11: (a) Selected surface samples and their images taken under confocal microscope; (b) Frequency-multiplier-based data modulation experiment setup; (c) Broadband THz time-domain system setup.

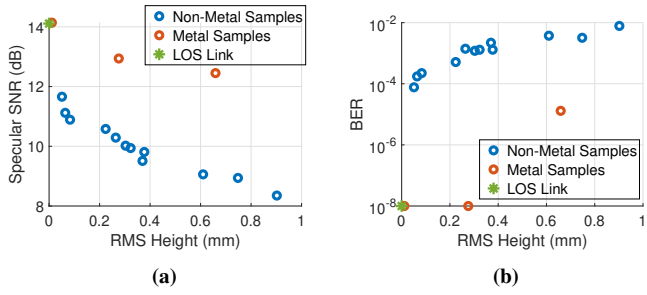
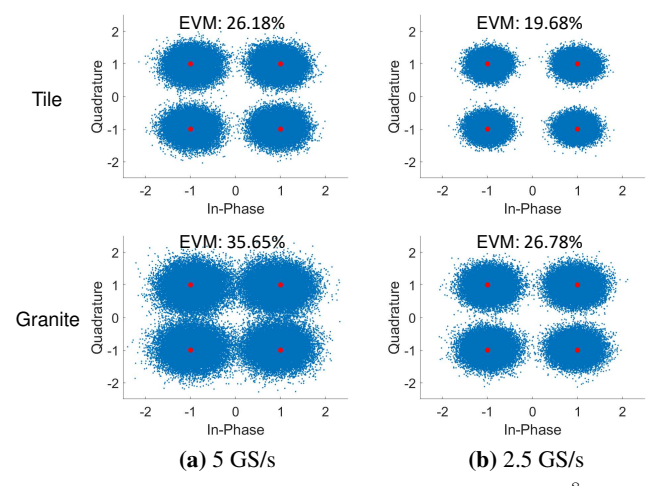


Fig. 12: The received SNR and BER for the LOS link and for NLOS links at the specular peak for different surface samples.

center of the surface covering an azimuth range of  $30^{\circ}-60^{\circ}$ . The signal detected by the RX is logged at every  $0.5^{\circ}$ .

We generate our IF signal using 4QAM modulation at a symbol rate of 5 GS/s. Given a pulse-shaping filter with a roll-off factor of  $\alpha=0.35$ , the IF signal occupies a bandwidth of 6.35 GHz. We center the IF signal at 5 GHz and configure our LO signal at 33.75 GHz. After up-conversion with a multiplication factor of  $4\times$ , the signal transmitted over-theair is centered at 140 GHz with a bandwidth of 6.35 GHz. The down-converted signal at the RX is observed on the oscilloscope for us to analyze the NLOS link from scattering off of each surface sample. At 140 GHz and an incident angle of  $45^{\circ}$ , surfaces are considered rough when their RMS heights are above 0.38 mm according to Rayleigh's criterion, below the roughness of some surface samples shown in Table I.

We first investigate the normalized SNR at specular angle  $\theta_s = 45^{\circ}$  for each surface sample as shown in Fig. 12(a). For very rough surfaces that create a random scattering profile with large perturbations, we record the maximum SNR in the range  $30^{\circ} < \theta_i < 60^{\circ}$ . We observe that the peak SNRs for both metal and non-metal samples exponentially decrease with higher  $h_{rms}$  values. The delta can be up to 4 dB between smooth and very rough surfaces. In general, this trend matches the model in Eq. (3). Another interesting observation is that the reflected power from metallic reference samples is much higher than that of non-metallic samples with similar roughness due to the difference in dielectric properties. However, the rate of SNR drop vs. RMS height is similar for all samples, implying that the contribution of roughness to SNR is independent of surface material. In addition, similar trends also apply to Fig. 12(b), which shows the BER of the specular NLOS link from 108 received bits. Evidently,



**Fig. 13:** Constellation diagram for tile and metal from 10<sup>8</sup> received bits at different symbol rates: (a) 5 GS/s and (b) 2.5 GS/s. Clear improvement in link quality is observed with lower bandwidth.

the specular link quality degrades monotonically with rougher reflectors. In addition, we also showed the received SNR and BER for a LOS link established at the same distance in Fig. 12, both of which are comparable to that for the specular NLOS link established with a smooth metal plate. These experimental results also demonstrate that despite the additional attenuation from reflection, it is indeed possible to establish a strong high-speed NLOS data link at sub-THz regime.

Further, we look deeper into the constellation plots for the two extreme cases of tile (very smooth) and granite (very rough) in Fig. 13. Particularly, we repeat the experiments at the symbol rate of 2.5 GS/s (corresponding to 3.375 GHz of bandwidth) and compare the constellation with the previous case of 5 GS/s. As expected, the error vector magnitude (EVM) of both reflected links improves under narrower bandwidths. Indeed, a smooth reflector can support a higher data rate given a fixed EVM performance requirement. The reason is two-fold: First, as discussed above, smooth reflectors provide higher SNR values. Second, the spectrum of a rough surface is frequency-selective due to non-coherent non-specular phase fronts. This implies that a smaller bandwidth should be chosen when a certain error performance goal is desired for a wireless system in an environment with rough reflectors.

We have experimentally demonstrated the possibility of establishing strong NLOS links with rough reflectors at 140

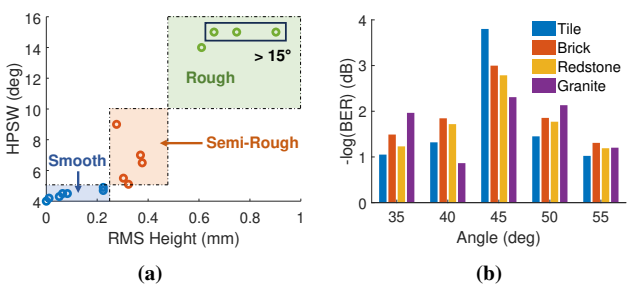


**Fig. 14:** Evaluating sensitivity of LOS and NLOS links against nodal motion. We show that (a) HPSW increases with surface RMS height, and (b) link quality is better maintained at non-specular angles for rougher surfaces.

GHz. In addition, we showed that the SNR performance of a specular NLOS link decreases nonlinearly with higher surface RMS height. We also observed that under NLOS link connectivity, the bandwidth of the link should be adapted based on the reflector roughness.

#### B. Mobility Resilient NLOS Links

Next, we experimentally investigate the scattering width off of rough surfaces and its implications for mobility-resilient NLOS links. We repeat the experiments from Sec. VI-A for all surface samples.

As explained in Sec. III-B, for NLOS links established with smooth surfaces, the received power should drop significantly with slight RX displacement while an evident increase in scattering width for the rough samples is expected. To demonstrate this trend, Fig. 14(a) shows the range of HPSW for different surface roughness categories. There is a positive relationship between surface RMS height and HPSW, suggesting better resilience against mobility for NLOS links established with rougher samples. Note that due to the extremely high surface perturbation of the granite sample, an irregular scattering shape is observed. Therefore, we expand the definition of HPSW to the angular width beyond which scattered power never raises above the -3-dB point from the peak power. Although there is a possibility of having a very wide scattering profile that generates a mobility-resilient beam, such unpredictable randomness in the scattering pattern makes it non-ideal to be selected as a reflector in a realistic wireless environment.

We notice that although the brick samples have  $3 \times$  higher RMS height compared to the tile samples, they show comparable scattering widths. Recall from Sec. III-B that for smooth surfaces with low  $h_{rms}$  below the Rayleigh's criterion, the scattering width changes slowly with  $h_{rms}$ . This observation suggests that mobility resilience in NLOS links only improves for reflectors beyond a certain roughness level.

In addition, we measure the BER at several non-specular angles  $(35^{\circ}, 40^{\circ}, 50^{\circ}, 55^{\circ})$  for each surface, and compare them with that for the specular link. The link quality (represented by -log(BER)) of each type of surface at different angles is shown in Fig. 14(b). At the specular angle, we observe an increase in BER for rougher surfaces. As we deviate from the specular angle, the data link established with rougher surfaces (i.e., brick, redstone, and granite) maintained a relatively

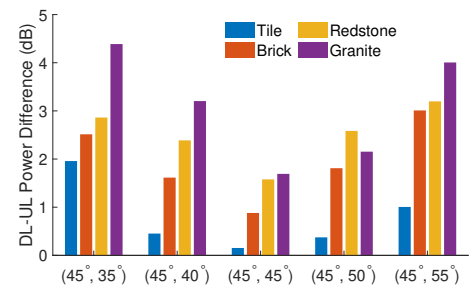


**Fig. 15:** The difference between the measured downlink and uplink SNR when swapping the TX and RX located at various angular configurations.

higher probability of receiving bits correctly. On the other hand, the links established from tile suffer more severely from angular displacement. These results imply better non-specular link qualities and therefore better mobility-resilience from scattering off of rough surfaces despite higher BER at the specular angle. Interestingly, for NLOS links established with the roughest granite, the BER does not increase uniformly toward non-specular angles. This implies a random scattering pattern for such surfaces.

NLOS links established with rough surfaces are more resilient against mobility due to a wider angular scattering profile. However, this comes at the cost of lower peak SNR, correspondingly higher specular BER, and possible highly random scattering shape.

#### C. Non-Reciprocal Beams

Next, we experimentally investigate beam reciprocity in NLOS links above 100 GHz. We measure the uplink and downlink signals by swapping the locations of TX and RX. Note that the spatial components (i.e. relative angles of the two nodes to the surface) of the channel remain unchanged.

Fig. 15 presents the differences between downlink and uplink power at multiple angular configurations averaged across the three samples for each material [1]. In our setup, the hardware front end of the TX and RX are identical. Hence, if beam reciprocity holds, the difference between received power under uplink and downlink should be negligible. However, we observe noticeable power differences in the order of a few dB, especially for rough surfaces such as granite. When both TX and RX are at 45° with respect to the reflector, the difference between the uplink and downlink beams is relatively small because the reflected beam is dominated by the coherent wavefront. Yet, we observe that as the NLOS link moves away from the specular direction, the power difference generally increases. Finally, we observe that the uplink/downlink power differences are higher for rougher samples. The only exception is that at  $(45^{\circ}, 50^{\circ})$ , the redstone sample has a higher uplink/downlink power difference than the granite sample. This is mainly due to the randomness in the non-coherent wavefront. This general trend follows our intuition in Sec. III-C because surface scattering profiles depend on the incident angle, which is a function of the transmitter location relative to the surface. At non-specular scattering angles ( $\theta_i \neq \theta_s$ ),

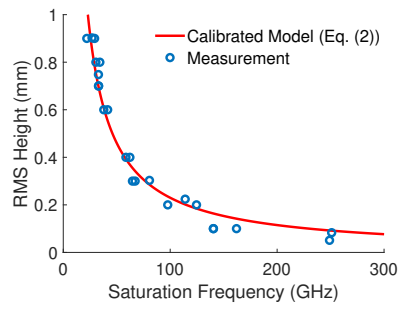


**Fig. 16:** The measured transition frequency  $f_{rough}$  from reflection spectra. We show highly accurate  $h_{rms}$  estimation with mean absolute error of 0.039 mm.

the scattering coefficient is different for uplink and downlink  $(\sigma(\theta_i, \theta_s) \neq \sigma(\theta_s, \theta_i))$ .

We have experimentally demonstrated that the presence of rough surfaces can challenge the assumption of TX/RX beam reciprocity. Wireless links established with rougher surfaces result in larger discrepancies between downlink and uplink power.

#### D. Performance of Surface Roughness Inference Framework

Finally, we evaluate our roughness estimation frameworks, i.e., the one-shot albeit ultra-wideband inference vs. few-shot narrowband roughness extraction.

Single-Shot Ultra-Wideband Estimation. First, we use our THz time-domain setup shown in Fig. 11(c) for fullband single-shot roughness extraction from specular reflection spectra. We place the THz transceiver at a normal incident angle and log the reflected signal. We normalize each received signal to the LOS case so that the effect of path loss in power spectra is eliminated. As discussed in Sec. IV-C, we inspect the spectrum of each reflected signal to extract the frequency transition signature, or  $f_{rough}$ , and estimate surface  $h_{rms}$ . As shown in Fig. 16, the measured  $f_{rough}$  and the ground truth RMS height of the surface samples agree well with the model obtained from Rayleigh's criterion, which is cross-verified with the wideband reflection spectra from both the IEM model as well as the EM simulations. We report an average absolute error of 0.039 mm. Despite its robust performance, it's not practical in wireless communication systems due to the need for transmission/detection in a prohibitively large swath of the spectrum. Nevertheless, this approach can be effective in certain sensing use cases such as industrial surface roughness characterization.

Few-Shot Inference from Spectral Variance. Next, we evaluate our few-shot roughness inference method that relies on mean spectral variance under different TX beams. Specifically, we emulate an IEEE 802.11ay-like downlink beam sweep procedure by angularly rotating the TX and keeping both TX and RX physically fixed at the specular angle of  $45^{\circ}$ . The center frequency is 140 GHz and the bandwidth is 20 GHz.

To estimate surface RMS height, we first log the power spectra of the qualified NLOS beams, and then calculate the mean spectral variance as discussed in Sec. IV-C. Fig. 17

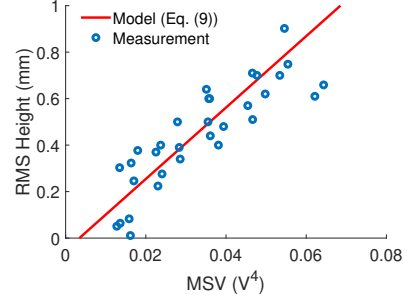


**Fig. 17:** The measured mean spectral variance of received spectra near the specular angle for natural everyday reflectors and select 3D-printed surfaces. There is a reasonable agreement between measured data, simulated data, and the fitted model in Sec. IV-C.

shows the measured MSV as a function of RMS height. We also plot our model that captures the relationship between MSV and RMS height according to Eq. (9). We find that our simulation-driven model is a good representative of the relationship between MSV and RMS height in practice. Note that for MSV calculation, we first normalize the power spectrum captured under each angular configuration to its peak as shown in Eq. (8); hence, we have removed the discrepancies in received power values in simulations vs. in measurements. In other words, MSV only captures the random spectral perturbation due to the non-coherent phase front which is a function of surface roughness and not the total received power. Therefore, our roughness estimation technique can be exploited in realistic wireless settings without prior calibration.

Finally, due to the lack of availability of real-life samples with intermediate roughness with  $h_{rms}$  values between 0.4 and 0.7 mm, we custom-designed and 3D printed 8 new random surface samples, with 2 surfaces at each  $h_{rms} =$ 0.4, 0.5, 0.6, and 0.7 mm. We repeated the measurement for these samples and calculated the corresponding MSV values to serve as test data. For all 15 real-life surfaces and the 8 additional 3D-printed samples we measure, we observe a mean absolute error of 0.101 mm and a median absolute error of 0.092 mm in  $h_{rms}$  estimation, comparable to that observed with the training data set from electromagnetic simulations shown in Fig. 9. Although less accurate than the resourcedemanding ultra-wideband estimation technique, this few-shot framework is more scalable, and such error has small impacts on the scattering patterns from a surface, which is the primary purpose of estimating surface roughness in sub-THz wireless networks.

Observing the smooth-rough transition from ultra-wideband reflection spectra produces 0.039 mm mean absolute error in RMS height estimation. In addition, the amount of spectral perturbation in sub-THz reflection measurements is also an accurate indicator of surface roughness. Our few-shot roughness estimation technique provides a mean absolute error of 0.101 mm in over-the-air experiments.

#### VII. RELATED WORK

**Surface Imaging.** Accurate imaging of rough surfaces has various applications in clinical diagnosis [29], security check [30], defect detection [31], archaeological analysis [32], and

interactive robotics [33]. Conventional systems utilize touch, laser, and vision-based sensors to track surface perturbations [34], [35]. Although these methods provide accurate surface profiling, they require specialized tools and equipment while imposing stringent requirements on the size and location of the surface. Recently, using wireless signals for surface imaging has become an area of increasing interest because of the ubiquity of wireless signals. Prior works leverage holographic arrays [36] and mmWave radar sensors [37] to capture surface perturbation. These efforts aim to reconstruct the surface height profile at the cost of high computation complexity and specialized hardware. However, estimating overall statistics of the surface perturbation would suffice for NLOS wireless communications. We emphasize that none of these imaging efforts has investigated the estimation of surface roughness in the context of wireless communications.

Rough Surface Scattering. The earliest efforts in modeling rough surface scattering for IR and UV wavelengths date back decades ago [38]. The Beckmann-Kirchhoff Model (KA) uses tangential surface fields to approximate scattering beam distribution [39], [12]. The small perturbation method (SPM) formulates scattering as a partial differential equation boundary value problem and is valid only for a small scale of surface roughness [12]. More complex models such as the small slope approximation (SSA), and the integral equation model (IEM) have also been introduced [7]. We take advantage of these models to understand the implication of rough surface scattering in sub-THz wireless networks.

Diffuse Scattering at THz. A few recent works looked at diffuse scattering above 100 GHz [3]. These works have mainly focused on the impact of rough surfaces on NLOS path loss [40], [41] and the possibility of establishing NLOS nonspecular links in THz wireless communications [8]. Different from past works, we further investigate the implications of diffuse scattering in transmit-receive beam reciprocity and mobility resilience with over-the-air communication links [42], [1]. Further, we propose two schemes for surface roughness statistics estimation. Our approaches infer roughness level via the unique spectral-spatial signatures captured in the spectra of received signals.

#### VIII. DISCUSSION

# Opportunities in Channel Modeling and Control Plane Design, Ray-tracing approaches have been commonly adopted

**Design.** Ray-tracing approaches have been commonly adopted for channel modeling for sub-THz wireless networks [43]. However, very few ray tracing models consider the additional propagation loss and non-specular components from rough surface scattering. Introducing the effect of scattering into ray-tracing models can substantially improve the channel modeling accuracy in sub-THz frequencies. To help with this line of work, we have made our dataset available online [44].

Meanwhile, the knowledge of rough surface scattering provides opportunities for wireless networking, such as choosing the optimum reflectors for establishing NLOS links. Given the tradeoff between the highest achievable data rate and better link reliability, a smooth reflector should be selected for stationary settings and when the data rate is prioritized. However,

a rough reflector should be selected to minimize mobility-induced link failures. Second, the lack of uplink/downlink beam reciprocity necessitates new beamforming strategies to find the best TX and RX beam configurations at a minimum time overhead. In addition, the frequency-selective scattering response also sheds light on bandwidth allocation and equalizer design. We will explore these research topics in the future.

Surface Roughness Sensing for Robotic Applications. Another opportunity for surface roughness sensing lies in robot grasping. The friction between a robot gripper and a target object is important to guarantee successful grasping. However, estimating friction information without contact remains an open challenge. Interestingly, surface roughness is directly correlated with the friction between surfaces. Using THz reflection to estimate surface roughness statistics (both surface RMS height and correlation length) at the area of contact between the robot gripper and the object opens a new realm for robot sensing. In addition, THz signals also have the potential for object and material identification, which can further enhance robot planning for grasping tasks. We leave this topic for future exploration.

#### IX. CONCLUSION

In this paper, we demonstrate the implications of rough scattering in sub-THz wireless networks and present a novel low-complexity scheme for surface roughness estimation. At this regime, the wavelength of wireless signals becomes comparable to minute surface height variations yielding rough scattering. Hence, reflection at sub-THz can yield patterns unique from that depicted by Snell's law. We investigate the impact of rough scattering on NLOS link strength, possibilities for strong non-specular links, mobility resilience, and beam reciprocity through a comprehensive discussion based on scattering theories and experimental analyses. In addition, we further exploit the spectral variations induced by the superposition of coherent and non-coherent wavefronts to estimate surface roughness statistics. Our approach is compliant with IEEE 801.11ay-like beam sweep protocols. Our over-the-air experiments demonstrate a mean absolute error of 0.101 mm.

# X. ACKNOWLEDGMENTS

This work was supported in part by the US National Science Foundation grants (CNS-2145240 and CNS-2313233), the US Air Force Office of Scientific Research (grant number FA9550-22-1-0382), and in part by the Center for Ubiquitous Connectivity (CUbiC), sponsored by Semiconductor Research Corporation (SRC) and Defense Advanced Research Projects Agency (DARPA) under the JUMP 2.0 program.

#### REFERENCES

- [1] R. Shen and Y. Ghasempour, "Scattering from rough surfaces in 100+ GHz wireless mobile networks: From theory to experiments," in *Proceedings of the 29th Annual International Conference on Mobile Computing and Networking*, ser. ACM MobiCom '23, 2023.
- [2] Y. Wu, J. Kokkoniemi, C. Han, and M. Juntti, "Interference and coverage analysis for terahertz networks with indoor blockage effects and line-of-sight access point association," *IEEE Transactions on Wireless Communications*, vol. 20, no. 3, pp. 1472–1486, 2021.

- [3] J. M. Jornet, E. W. Knightly, and D. M. Mittleman, "Wireless communications sensing and security above 100 ghz," *Nature Communications*, vol. 14, no. 1, 2023.
- [4] Y. Ghasempour, Y. Amarasinghe, C.-Y. Yeh, E. Knightly, and D. M. Mittleman, "Line-of-sight and non-line-of-sight links for dispersive terahertz wireless networks," APL Photonics, vol. 6, no. 4, p. 041304, 2021.
- [5] J. Ma, R. Shrestha, L. Moeller, and D. M. Mittleman, "Invited article: Channel performance for indoor and outdoor terahertz wireless links," *APL Photonics*, vol. 3, no. 5, p. 051601, Feb 2018.
- [6] S. R. Brown and C. H. Scholz, "Broad bandwidth study of the topography of natural rock surfaces," *Journal of Geophysical Research: Solid Earth*, vol. 90, no. B14, pp. 12575–12582, 1985.
- [7] A. K. Fung and K. S. Chen, Microwave Scattering and Emission Models and Their Applications. Artech House, 1994.
- [8] J. Ma, R. Shrestha, W. Zhang, L. Moeller, and D. M. Mittleman, "Terahertz wireless links using diffuse scattering from rough surfaces," *IEEE Transactions on Terahertz Science and Technology*, vol. 9, no. 5, pp. 463–470, 2019.
- [9] Y. Ghasempour, C. da Silva, C. Cordeiro, and E. W. Knightly, "IEEE 802.11ay: Next-generation 60 GHz Communication for 100 Gbps Wi-Fi," *IEEE Communications Magazine*, vol. 55, no. 12, pp. 186–192, 2017.
- [10] J. Ku, J.W. Strutt, Third Baron Rayleigh, The Theory of Sound, First Edition (1877–1878), 12 2005, pp. 588–599.
- [11] O. Landron, M. Feuerstein, and T. Rappaport, "A comparison of theoretical and empirical reflection coefficients for typical exterior wall surfaces in a mobile radio environment," *IEEE Transactions on Antennas and Propagation*, vol. 44, no. 3, pp. 341–351, 1996.
- [12] F. T. Ulaby, Microwave Remote Sensing. Artech House, 1981.
- [13] L. Tsang, J. A. Kong, and R. T. Shin, Theory of microwave remote sensing. John Wiley & Sons, 1985.
- [14] A. K. Fung, W. Y. Liu, K. S. Chen, and M. K. Tsay, "An improved iem model for bistatic scattering from rough surfaces," *Journal of Electromagnetic Waves and Applications*, vol. 16, no. 5, pp. 689–702, 2002
- [15] F. Ticconi, L. Pulvirenti, and N. Pierdicca, "Models for scattering from rough surfaces," in *Electromagnetic Waves*, V. Zhurbenko, Ed. Rijeka: IntechOpen, 2011, ch. 10.
- [16] E. N. Papasotiriou, A.-A. A. Boulogeorgos, K. Haneda, M. F. de Guzman, and A. Alexiou, "An experimentally validated fading model for thz wireless systems," *Scientific Reports*, vol. 11, no. 1, 2021.
- [17] M. M. Rahman, M. S. Moran, D. P. Thoma, E. E. S. R. Bryant, C. D. H. Collins, S. Skirvin, C. Kershner, and B. J. Orr, "A derivation of roughness correlation length for parameterizing radar backscatter models," *International Journal of Remote Sensing*, vol. 28, no. 18, pp. 3995–4012, 2007.
- [18] E. Altese, O. Bolognani, M. Mancini, and P. A. Troch, "Retrieving soil moisture over bare soil from ers 1 synthetic aperture radar data: Sensitivity analysis based on a theoretical surface scattering model and field data," Water Resources Research, vol. 32, no. 3, pp. 653–661, 1996.
- [19] J. R. Carson, "Reciprocal theorems in radio communication," Proceedings of the Institute of Radio Engineers, vol. 17, no. 6, pp. 952–956, 1979
- [20] Y. Ghasempour, M. K. Haider, and E. W. Knightly, "Decoupling Beam Steering and User Selection for MU-MIMO 60 GHz WLANs," *IEEE/ACM Transactions on Networking*, vol. 26, no. 5, pp. 2390–2403, 2018.
- [21] Federal Communications Commission, "James Edwin Whedbee Petition for Rulemaking to Allow Unlicensed Operation in the 95-1,000 GHz Band," ET Docket, vol. 26, no. 18-21, Mar. 2019.
- [22] T. Nitsche, C. Cordeiro, A. B. Flores, E. W. Knightly, E. Perahia, and J. C. Widmer, "Ieee 802.11ad: Directional 60 ghz communication for multi-gigabit-per-second wi-fi [invited paper]," *IEEE Communications Magazine*, vol. 52, no. 12, pp. 132–141, 2014.
- [23] L. L. Yang, "60ghz: Opportunity for gigabit wpan and wlan convergence," vol. 39, no. 1, p. 56–61, 2009.
- [24] T. S. Rappaport, Y. Xing, O. Kanhere, S. Ju, A. Madanayake, S. Mandal, A. Alkhateeb, and G. C. Trichopoulos, "Wireless communications and applications above 100 ghz: Opportunities and challenges for 6g and beyond," *IEEE Access*, vol. 7, pp. 78729–78757, 2019.
- [25] S. Farjana, M. Ghaderi, A. U. Zaman, S. Rahiminejad, T. Eriksson, J. Hansson, Y. Li, T. Emanuelsson, S. Haasl, P. Lundgren, and et al., "Realizing a 140 ghz gap waveguide-based array antenna by low-cost injection molding and micromachining," *Journal of Infrared, Millimeter, and Terahertz Waves*, vol. 42, no. 8, p. 893–914, Sep 2021.

- [26] Y. Ghasempour, R. Shrestha, A. Charous, E. Knightly, and D. M. Mittleman, "Single-Shot Link Discovery for Terahertz Wireless Networks," *Nature Communication*, vol. 11, no. 1, p. 2017, 2020.
- [27] A. Ahmed, L. Li, M. Jung, and G. M. Rebeiz, "A 140 ghz scalable on-grid 8x8-element transmit-receive phased-array with up/down converters and 64qam/24 gbps data rates," in 2023 IEEE Radio Frequency Integrated Circuits Symposium (RFIC), 2023, pp. 93–96.
- [28] U. Ugurlu, R. Wichman, C. B. Ribeiro, and C. Wijting, "A multipath extraction-based csi acquisition method for fdd cellular networks with massive antenna arrays," *IEEE Transactions on Wireless Communica*tions, vol. 15, no. 4, pp. 2940–2953, 2016.
- [29] M. Eder, G. Brockmann, A. Zimmermann, M. A. Papadopoulos, K. Schwenzer-Zimmerer, H. F. Zeilhofer, R. Sader, N. A. Papadopulos, and L. Kovacs, "Evaluation of precision and accuracy assessment of different 3-d surface imaging systems for biomedical purposes," *Journal* of Digital Imaging, vol. 26, no. 2, p. 163–172, 2012.
- [30] Y. Cheng, Y. Wang, Y. Niu, and Z. Zhao, "Concealed object enhancement using multi-polarization information for passive millimeter and terahertz wave security screening," *Optics Express*, vol. 28, no. 5, p. 6350, 2020.
- [31] S. Ghorai, A. Mukherjee, M. Gangadaran, and P. K. Dutta, "Automatic defect detection on hot-rolled flat steel products," *IEEE Transactions on Instrumentation and Measurement*, vol. 62, no. 3, pp. 612–621, 2013.
- [32] G. C. Walker, J. W. Bowen, J. B. Jackson, W. Matthews, J. Labaune, G. Mourou, M. Menu, and I. Hodder, "Sub-surface terahertz imaging through uneven surfaces: Visualizing neolithic wall paintings in Çatalhöyük," in 2012 Conference on Lasers and Electro-Optics (CLEO), 2012, pp. 1–2.
- [33] Y. Yamamoto, P. Pirjanian, M. Munich, E. DiBernardo, L. Goncalves, J. Ostrowski, and N. Karlsson, "Optical sensing for robot perception and localization," in *IEEE Workshop on Advanced Robotics and its Social Impacts*, 2005., 2005, pp. 14–17.
- [34] T. Kamigaki, K. Nakatsuma, Y. Oshima, and I. Torigoe, "Detection of ultrasound pressure distribution for remote measurement of haptic surface roughness," in 2015 IEEE SENSORS, 2015, pp. 1–4.
- [35] Y. Liu, S. Lu, and H. Culbertson, "Texture classification by audio-tactile crossmodal congruence," in 2022 IEEE Haptics Symposium (HAPTICS), 2022, pp. 1–7.
- [36] Y. Rahmat-Samii and J. Lemanczyk, "Application of spherical near-field measurements to microwave holographic diagnosis of antennas," *IEEE Transactions on Antennas and Propagation*, vol. 36, no. 6, pp. 869–878, 1988.
- [37] P. A. Scharf, M. A. Mutschler, J. Iberle, H. Mantz, T. Walter, and C. Waldschmidt, "Spectroscopic estimation of surface roughness depth for mm-wave radar sensors," in 2019 16th European Radar Conference (EuRAD), 2019, pp. 93–96.
- [38] H. Davies, The Reflection of Electromagnetic Waves from a Rough Surface. Proceedings of the Institute of Electrical Engineers, 1954.
- [39] P. Beckmann and S. Andre, The Scattering of Electromagnetic Waves from Rough Surfaces. Pergamon Press, 1963.
- [40] J. Kokkoniemi, J. Lehtomäki, and M. Juntti, "Measurements on rough surface scattering in terahertz band," in 2016 10th European Conference on Antennas and Propagation (EuCAP), 2016, pp. 1–5.
- [41] D. Serghiou, M. Khalily, S. Johny, M. Stanley, I. Fatadin, T. W. C. Brown, N. Ridler, and R. Tafazolli, "Comparison of diffuse roughness scattering from material reflections at 500-750 ghz," in 2021 15th European Conference on Antennas and Propagation (EuCAP), 2021, pp. 1–5.
- [42] R. Shen and Y. Ghasempour, "Rough surfaces scattering and mobility-resilient terahertz wireless links," in 2023 48th International Conference on Infrared, Millimeter and Terahertz Waves (IRMMW-THz), 2023, pp. 1–2
- [43] H. Poddar, S. Ju, D. Shakya, and T. S. Rappaport, "A tutorial on nyusim: Sub-terahertz and millimeter-wave channel simulator for 5g, 6g and beyond," *IEEE Communications Surveys & Tutorials*, pp. 1–35, 2023.
- [44] R. Shen, "Sub-terahertz rough surface scattering measurement," 2024. [Online]. Available: https://dx.doi.org/10.21227/s5f6-fs33



Ruiyi Shen (Graduate Student Member, IEEE) received the B.S. degree in electrical engineering from University of Southern California (USC), Los Angeles, CA, USA, in 2022, and the M.A. degree from Princeton University, Princeton, NJ, USA, in 2024, where he is currently pursuing the Ph.D. degree at the Department of Electrical and Computer Engineering. His research interests include the design and evaluation of novel physical layer architecture and protocols for next-generation mmWave and sub-THz wireless communication and sensing systems.

Ruiyi Shen graduated with honors at the B.S. degree, and he is a recipient of the Pramod Subramanyan \*17 Early Career Graduate Award from Princeton University in 2024.



Yasaman Ghasempour (Member, IEEE) is an Assistant Professor of Electrical and Computer Engineering at Princeton University. She received her Ph.D. and master's degree from Rice University and her bachelor's degree from the Sharif University of Technology. Yasaman Ghasempour is the recipient of the NSF CAREER Award (2022), the 2024 AFOSR YIP Award, the 2020 Marconi Young Scholar Award, the E. Lawrence Keys, Jr./Emerson Electric Co. Faculty Award (2024), and the Excellence in Teaching Award (Princeton SEAS). She is

listed as one of 10 rising stars worldwide in Computer Networking and Communications in 2022. Her group received the best paper award in USENIX NSDI 2023 and ACM MobiCom 2023. Yasaman Ghasempour is featured in the Smithsonian Institution's Museum of Natural History as a change-making innovator in wireless technology. Her research is focused on next-generation wireless networks and sensing systems, including novel devices and protocols for millimeter-wave and terahertz WLANs.